Ultrahigh resolution spectral-domain optical coherence tomography using the 1000–1600 nm spectral band

LIANE BERNSTEIN,[1,2] **ANTOINE RAMIER,**[1,3] **JIAMIN WU,**[1,4,5] **VERA D. AIELLO,**[6] **MARIE J. BÉLAND,**[7] **CHARLES P. LIN,**[1,8] **AND SEOK-HYUN YUN**[1,3,8,*]

[1]*Wellman Center for Photomedicine, Massachusetts General Hospital, 50 Blossom Street, Boston, MA 02140, USA*
[2]*Department of Electrical Engineering and Computer Science, Massachusetts Institute of Technology, Cambridge, MA, USA*
[3]*Health Sciences and Technology, Massachusetts Institute of Technology, Cambridge, MA, USA*
[4]*Department of Automation, Tsinghua University, Beijing 100084, China*
[5]*Institute for Brain and Cognitive Science, Tsinghua University, Beijing 100084, China*
[6]*Laboratory of Pathology, Heart Institute, University of São Paulo Medical School, São Paulo, Brazil*
[7]*Division of Pediatric Cardiology, The Montreal Children's Hospital of the McGill University Health Centre, Montréal, Quebec, Canada*
[8]*Department of Dermatology, Harvard Medical School, Boston, MA, USA*
[*]*syun@mgh.harvard.edu*

Abstract: Ultrahigh resolution optical coherence tomography (UHR-OCT) can image microscopic features that are not visible with the standard OCT resolution of 5-15 µm. In previous studies, high-speed UHR-OCT has been accomplished within the visible (VIS) and near-infrared (NIR-I) spectral ranges, specifically within 550-950 nm. Here, we present a spectral domain UHR-OCT system operating in a short-wavelength infrared (SWIR) range from 1000 to 1600 nm using a supercontinuum light source and an InGaAs-based spectrometer. We obtained an axial resolution of 2.6 µm in air, the highest ever recorded in the SWIR window to our knowledge, with deeper penetration into tissues than VIS or NIR-I light. We demonstrate imaging of conduction fibers of the left bundle branch in freshly excised porcine hearts. These results suggest a potential for deep-penetration, ultrahigh resolution OCT in intraoperative applications.

1. Introduction

Optical coherence tomography (OCT) has been widely used in Ophthalmology and is gaining adoption in Interventional Cardiology and other medical fields for diagnosis and treatment monitoring. Commercial diagnostic OCT systems have a typical axial resolution of 5 to 15 µm. Much higher resolution, up to ~1 µm, has been demonstrated in the research community by using a broader optical bandwidth spanning nearly half an octave [1–10]. This ultrahigh resolution OCT (UHR-OCT), although instrumentally more complex, is needed to examine cellular-level features that are not easily visible in conventional-resolution OCT. Most of these UHR-OCT systems have been realized in the spectral-domain (SD) system architecture and use broadband light sources, such as femtosecond Ti:sapphire lasers, cascaded superluminescent diodes, or supercontinuum light sources. They operate in subregions of the visible (VIS) to first near-infrared (NIR-I) wavelength bands: specifically, their bandwidths fall within 550 to 950 nm, a range well-supported by silicon-based detectors. The use of relatively short wavelengths is advantageous in terms of axial resolution, as the coherence length of light decreases with the square of its center wavelength. However, for deep imaging in highly scattering tissues, longer wavelengths — NIR-II spanning from 1000 to 1400 nm and NIR-III from 1500 to 1800nm, collectively known as

Short-Wavelength Infrared (SWIR) — are preferred to the NIR-I range [11]. In biological tissues, the magnitude of light scattering decreases as wavelength increases [12,13], which results in improved signal-to-noise ratio (SNR). Furthermore, the maximum permissible optical power for tissues is higher in the SWIR, where photochemical damage risk is low [14]. Earlier efforts to realize UHR-SD-OCT in the SWIR have had resolutions of at best 4-5 μm [11,15–19]. Other UHR-OCT systems have been limited to the time-domain (TD) architecture, for example, using a 470 nm-bandwidth source at a central wavelength of 1375 nm [20], 350 nm bandwidth at 1300 nm [21], 370 nm bandwidth at 1300 nm [22], or 420 nm bandwidth at 1320 nm [23]. Since TD-OCT has intrinsic drawbacks in SNR, these systems offer substantially lower penetration depths and imaging speeds compared to SD-OCT systems [24–26].

Here, we demonstrate a UHR-SD-OCT system using a spectral range from 1000 to 1600 nm. We achieve an axial resolution of 2.6 μm in air, the highest ever shown to our knowledge in the SWIR range. We demonstrate the feasibility of the potential application of our device to the identification of conductive fiber bundles in cardiac tissues.

2.   OCT system: design and characterization

Figure 1 shows a schematic of our UHR-SD-OCT system. The light source is a supercontinuum laser (NKT Photonics SuperK EXTREME EXW-4). Its two-octave-spanning single-mode output beam is attenuated by a neutral-density (ND) filter and then filtered by a 980 nm longpass filter (Semrock BLP01-980R-25) in the source arm. A 50/50 beamsplitter divides the input light into the reference and sample arms. The sample arm includes a pair of galvanometric (galvo) steering mirrors (Thorlabs GVS012) for raster scanning on a sample, relay achromatic doublet lenses (Thorlabs AC508-100-C) and an objective lens (Olympus LMPLN5XIR, numerical aperture (NA) of 0.1, underfilled, focal length f of 36 mm). The lens positions are adjusted such that the galvo mirrors are approximately imaged to the back focal plane of the objective lens. The reference arm employs the same relay lenses and a similar objective lens as the sample arm for chromatic dispersion compensation. The objective lens produces a lateral resolution of 15 μm in air (see Supplement 1, section 1). This relatively low resolution was chosen to maintain a long depth of focus. In the detection arm, an off-axis parabolic mirror (Edmund Optics 37-295) focuses light into a single-mode photonic crystal fiber (PCF, Newport F-SM8-C-2FCA). The PCF acts as a pinhole to reject out-of-focus light from the sample and transmits the signal to a home-built spectrometer. The spectrometer consists of a grating with 600 lines/mm (Wasatch Photonics WP-600/1550-25.4), off-the-shelf achromatic, plano-convex and meniscus lenses (Thorlabs AC508-080-C, LA1417-C, and LE1418-C) chosen for low combined aberration and a 2048-pixel InGaAs camera with a tunable linescan speed up to 147,000 lines per second (147 klps, Sensors Unlimited GL2048R). See Supplement 1, sections 1 and 2 for system design, theoretical limits and ray-tracing spectrometer simulation. The camera output is transferred to a computer via a Camera Link frame grabber (Matrox Solios eV-CL) and processed with custom-written software for both real-time and post image processing (see Supplement 1, section 3). The computer also has an analog/digital output board (National Instruments) to control the galvo mirrors and camera.

The light source power was set to a manufacturer-calibrated 48% level (unfiltered output power ~1 W) at which the optical spectrum recorded in the spectrometer exhibited a desirable round shape in the SWIR range (Fig. 2(a)). The ND filter in the source arm was selected to make the total power at the sample 25 mW (see Supplement 1, section 4 for discussion on maximum permissible power level for non-retinal tissue imaging). The variable ND filter in the reference arm was adjusted so that the reference-arm light filled approximately half the pixel well depth in the camera. Figure 2(b) shows an example interferogram from a partial reflector sample to illustrate good visibility across the entire bandwidth from 1000 to 1600 nm.
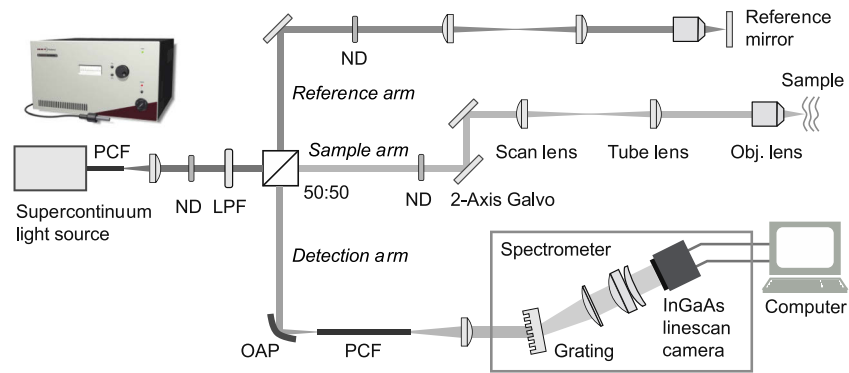
Fig. 1. Schematic of our ultrahigh-resolution SD-OCT system operating in a spectral range of 1000-1600 nm from a supercontinuum light source. ND: neutral density filter, LPF: longpass filter (980 nm), scan and tube lenses: $f = 100$ mm, objective lens: $5\times$ ($f = 36$ mm), OAP: off-axis parabolic mirror ($f = 12.7$ mm), PCF: photonic crystal fiber and grating: 600 lines/mm.
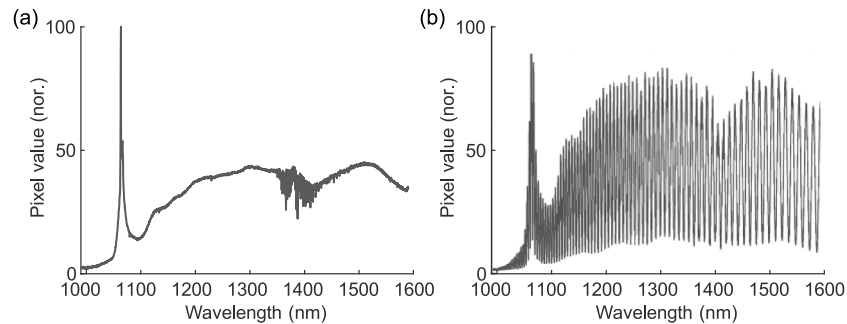

Fig. 2. (a) Reference arm spectrum measured on our custom spectrometer (sample arm blocked). (b) Example interference signal recorded when the optical power levels from the sample and reference arms were deliberately made equal.

To measure our system's sensitivity and axial resolution, we placed a mirror in the sample position (with optical power 25 mW) and then rotated the variable ND filter in the sample arm from full transmission to 30 dB attenuation. Figure 3 shows reflectivity profiles after processing (including windowing) measured at different path length delays, where the objective lens and reference mirror were translated together in the reference arm, with a camera readout speed of 10 klps. The decrease in SNR with increasing path length difference is called sensitivity roll-off. This effect is primarily due to the finite spectral resolution of the spectrometer, which reduces fringe visibility at higher spatial frequencies and thus also broadens the point spread functions (PSFs) at longer path length delays [27,28]. The 3-dB roll-off depth is measured to be 0.5 mm, and the decrease in signal strength at a delay of 1.2 mm (90% of the maximum measurement depth) is 16 dB (Fig. 3(a)). From the full width at half maximum of the coherence envelope, i.e., the Fourier transform of the processed interferogram [29], the axial resolution is 2.6 µm in air at a delay of 40 µm (Fig. 3(b)) and remains below 3.0 µm until a delay of 0.6 mm; at a delay of 1.2 mm, the resolution worsens to 4.2 µm. The SNR is measured to be ~44 dB at a delay of 40 µm (Fig. 3(c)). Factoring in the effective reflectivity of the sample (-60 dB), the sensitivity of the system is therefore ~104 dB. This value is ~10 dB lower than the theoretical shot-noise limited sensitivity and is largely due to the high relative intensity noise of the source light [30]. See

Supplement 1, section 5 for a discussion on our choice of window and its impact on resolution, sidelobes and sensitivity.
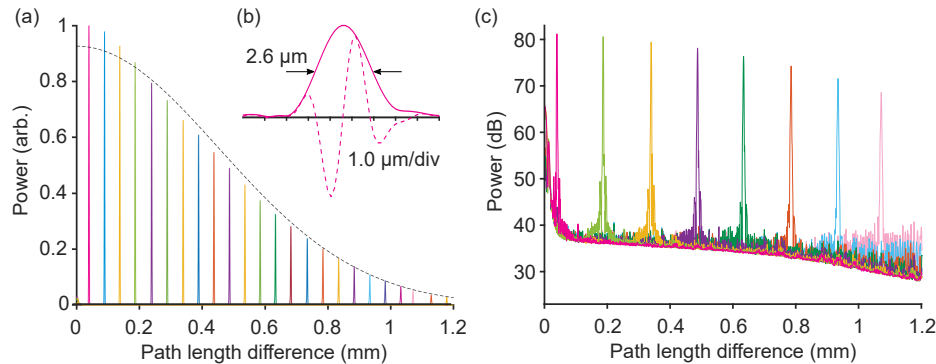

Fig. 3. Measured reflectivity profiles of a -60 dB reflector at different delay depths. 2,000 A-lines acquired at a rate of 10 klps were incoherently averaged at each mirror position for better visualization of the noise floor. (a) Linear scale, normalized. Dashed black line: fitted theoretical curve. (b) Point spread function (PSF) at a delay of 40 μm (linear scale). Dashed curve: real part of PSF; solid curve: absolute value of PSF (envelope). (c) Same as (a), log scale.

We also measured the system's sensitivity at the maximum camera readout rate of 146 klps, at which the pixel integration time is 4.5 μs. The sensitivity dropped to 84 dB, which is 7.6 dB lower than what is expected solely from the difference in pixel integration time. This discrepancy is thought to be due in part to excess electrical noise of the camera at high readout speed and in part to high frequency relative intensity noise of the light source. All OCT imaging experiments described below were performed at 10 klps. Each cross-sectional image (B-scan) was composed of ~1,600 A-lines and was acquired in ~0.2 s, including galvo turn-around time.

For a comparison to conventional-resolution OCT, we imaged a roll of semi-transparent tape (3M, Scotch Magic tape) using both our UHR-SD-OCT system and a standard swept-source OCT system available in our laboratory. The standard OCT system uses a wavelength-swept laser in a spectral range of 1250-1380 nm and has axial and lateral resolutions of ~15 μm and
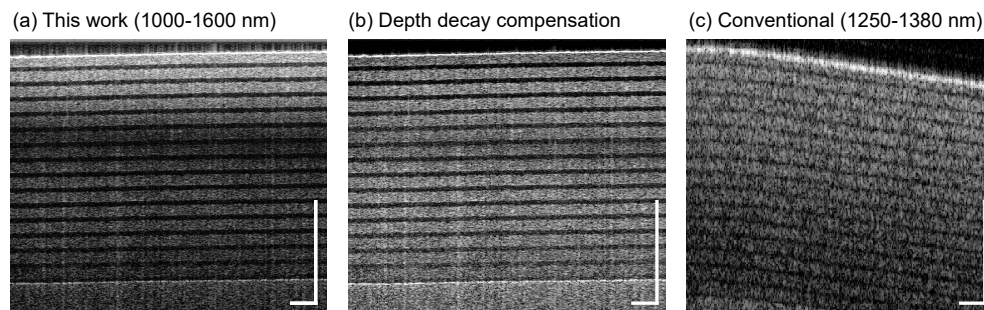

Fig. 4. Cross-sectional OCT images of a tape roll. (a) UHR-SD-OCT image with subtraction of autocorrelation and binning (sum) of five lateral pixels per A-line. Dynamic range: 42 dB. (b) Same image as (a), but with additional depth-decay compensation (from an average of all A-lines, calculate a piece-wise linear fit of maxima of each strip of tape versus depth and subtract the fit from each A-line). Dynamic range: 34 dB. (c) Image of same sample acquired with a standard-resolution SS-OCT system centered at 1350 nm; no binning or subtraction of autocorrelation, 615 A-lines. Dynamic range: 50 dB. Scale bars: 500 μm.

~30 μm, respectively, with a sweep rate of 45 kHz. In Fig. 4, the high axial resolution of our UHR-SD-OCT system is clearly visible, with sharp contrast between the different layers of tape, as compared with the standard OCT system, where they are blurred. An autocorrelation image
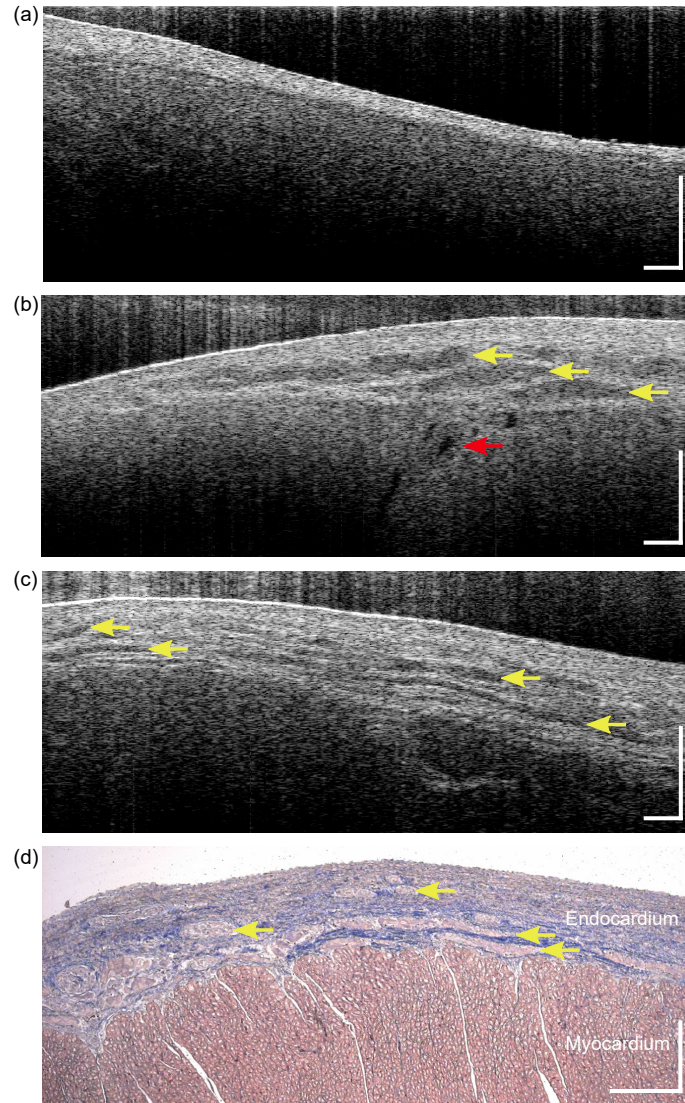

Fig. 5. (a) Cross-sectional UHR-SD-OCT image of membranous septum imaged from left ventricular aspect of a porcine heart. (b) Cross-sectional UHR-SD-OCT image of an area of the left ventricular outlet septum in the same heart immediately below the membranous septum and below the aortic valve, showing the transition from the membranous septum to conduction tissue in left bundle branch. Yellow arrows indicate conduction fibers of the left bundle branch, red arrow indicates an arteriole. See Visualization 1 and Visualization 2 for animated XZ and YZ (resliced) stacks as well as Dataset 1 [31] for full-resolution XZ stack. (c) Cross-sectional UHR-SD-OCT image from a similar area of a second freshly explanted porcine heart. Arrows indicate conduction fibers of the left bundle branch. (d) Histology slide dyed with Masson's trichrome of left bundle branch in porcine heart. Light pink regions within endocardium: conduction fibers of the left bundle branch (also labeled with arrows); blue: collagen; dark pink: muscle (myocardium). Dynamic range in (a-c): 33 dB, binning of three lateral pixels per A-line. Scale bars: 300 μm.

was acquired by blocking the reference arm, and this autocorrelation was subtracted from the signal in Fig. 4(a) and (b) to reduce noise (however, this autocorrelation subtraction was not performed in Fig. 5). The vertical scale bars here and in the rest of the paper are in units of optical path length mismatch between the sample and reference arms since the exact refractive index of each material is not known.

3. Imaging cardiac tissues and conduction fibers

In the human heart, specialized conduction pathways bring action potentials from the atria to the ventricles to trigger myocardial contractions [32]. Normally, action potentials originating in the sinoatrial (SA) node located high in the right atrium propagate through atrial muscle to the atrioventricular (AV) node, located in the lower right atrium near the right AV junction. The action potentials are then conducted to the ventricles via a bundle of specialized fibers known as the bundle of His or AV bundle. Having penetrated into the ventricles through the central fibrous body of the heart, the AV bundle reaches the left lower edge of the membranous part of the ventricular septum and divides into the left and the right bundle branches which descend on either side of the muscular ventricular septum. These bundle branches then ramify into fine Purkinje fibers, which ultimately transmit the action potentials to ventricular muscle cells to trigger a ventricular contraction. A distinguishing feature of the mammalian heart is that the specialized conduction tissues (AV bundle and bundle branches) are wrapped in a sheath of fibrous tissue which insulates them from the surrounding myocardium, thus preventing early depolarization of the basal myocardium. While this fibrous envelope is useful to identify the atrioventricular conductive bundles histologically, these bundles are not visible to the naked eye.

In the presence of congenital heart disease, AV conduction fibers may have an abnormal course. One of the most common congenital cardiac malformations is a ventricular septal defect (VSD), a hole in the wall separating the two ventricles. In many cases, the VSD involves the membranous part of the ventricular septum where the AV bundle may run for a variable length along the edge of the defect. Because the AV bundle and bundle branches are not visible to the surgeon, the conduction fibers may inadvertently be injured during patch closure of such defects. Heart block can ensue, which may necessitate the implantation of a permanent pacemaker since the AV node represents the only conduction pathway between the atria and the ventricles. A recent retrospective study of over 100,000 open heart surgeries in pediatric patients showed that in 1% of cases, surgery caused heart block. Furthermore, heart block was associated with higher odds of mortality [33]. The development of an intraoperative tool that allows a surgeon to visualize the location of the AV conduction pathway relative to the defect that is being repaired could therefore potentially be of great importance in reducing mortality and long-term pacemaker use, particularly in pediatric congenital heart surgery [34].

Previously, a standard-resolution time-domain OCT system centered at 1310 nm was tested for imaging the SA nodal region of an *ex vivo* canine heart [35]. In another study, the visualization by standard-resolution OCT of the AV node in freshly explanted porcine hearts was described [36]. In both cases, the amorphous and non-encapsulated nature of both nodes likely hampered the clear delineation of these structures by OCT. Purkinje fibers, which are demarcated histologically by a fibrous sheath, were more clearly observed by Yao et al. [7] in an *ex vivo* porcine heart with a UHR-SD-OCT system centered at 840 nm with an axial resolution of 2.7 μm. In this work by Yao et al. [7], the authors compare their system's imaging of porcine heart tissue with that of a commercial system centered at 1300 nm; though their device resolves finer features, the penetration depth is greater with the longer-wavelength commercial system. We reasoned that ultrahigh resolution OCT in the SWIR range with greater penetration depth may enable the mapping of similarly sheathed cardiac conductive pathways within the endocardium, such as the AV bundle and bundle branches.

To test the feasibility of visualizing these cardiac conduction tissues with our UHR-SD-OCT system, we imaged freshly excised porcine hearts (a common model for the human heart [37]) in the region where the left bundle branch emerges on the left side of the heart, just below the membranous septum. Porcine hearts were obtained immediately after death from a local slaughterhouse (Research 87, Boylston, MA). The MGH Institutional Research Safety Committee approved the use of biological samples. To locate the thin membranous septum, the porcine heart was trans-illuminated from the right ventricular side, and, as observed from the left side beneath the aorta, the membranous septum was identified near the mitral valve (see photo in Supplement 1, section 6). Figure 5(a) shows a UHR-SD-OCT image of the membranous septum, where the endocardial layer is seen without any noticeable features, as this region does not have arteries or fiber bundles. We then translated the sample to visualize conduction fibers within the left bundle branch, as well as deeper features within the myocardium such as an arteriole, as shown in Fig. 5(b). Also see Dataset 1 [31] for the acquired image stack of this region (full resolution) and Visualizations 1 and 2 for animated XZ and YZ (resliced) stacks (downsampled due to constraints on file size). Figure 5(c) shows a UHR-SD-OCT image from a similar area in a second porcine specimen with densely packed conduction fibers of the left bundle branch. Compared to Fig. 4, penetration depth was limited here due to the higher attenuation of light in heart tissue versus tape. Figure 5(d) shows a histological section with Masson's trichrome staining of a similar region of a porcine heart, showing good correspondence to Fig. 5(b) and (c).

4. Discussion

A number of improvements in image quality could be made to the system. The sensitivity can be significantly enhanced by using more advanced supercontinuum sources with lower relative intensity noise, such as those using an all-normal-dispersion fiber [38] or on-chip silicon nitride waveguide [39]. Part of this improved sensitivity could then be used to operate the spectrometer camera at its full acquisition rate. Autocorrelation induces the vertical streaks seen in the images in Fig. 5; we did not subtract the autocorrelation noise to illustrate the "single-shot" capability of our system that may be preferred in an intraoperative context. On the other hand, a number of simple, high-speed techniques have been proposed to eliminate these artifacts, for example, with an optical switch in the reference arm to enable acquisition and subtraction of an autocorrelation image [40]. The autocorrelation noise is most prominent when the reflected power from the sample is too high for a given reference power; these artifacts could be reduced with better index matching at the surface, e.g., by applying drops of phosphate buffered saline. We also note a decrease in axial resolution with depth in our images, which can be attributed in part to the finite spectral resolution of the spectrometer, as described in section 2. A lens that focuses more tightly onto a line camera with a greater number of pixels can lessen this effect. In-depth axial resolution is also affected by the optical properties of biological tissues, where the optical bandwidth is reduced by wavelength-dependent attenuation via scattering of shorter wavelengths and absorption by water in the ~1400-1500 nm band. Lastly, dispersion in the sample leads to dispersion mismatch between the sample and reference arms (our numerical dispersion compensation is only valid at the sample surface). More advanced algorithms can correct for dispersion mismatch at multiple interfaces (e.g., [18]). The lateral resolution can be enhanced by using an objective lens of higher NA with a Bessel beam or synthetic aperture to maintain the axial DOF [2,41].

The 2.6-μm axial resolution of our system, measured in air, is the highest achieved in the SWIR band, to our knowledge. This combination of high resolution and deeper penetration in highly scattering tissues may enable novel non-invasive medical imaging. In this paper, we have proposed an intraoperative application to image the cardiac conduction system, and our system resolved microscopic features such as conduction fibers of the left bundle branch of two normal porcine hearts. Polarization sensitivity may enhance the contrast of the cardiac conduction fibers

further since they are rich in collagen and thus optically birefringent. We hypothesize that our system could be used to locate AV conduction tissues, of a similar structure to the conductive fibers of the left bundle branch, as they run close to the margins of defects in the presence of certain types of VSDs [42,43]. In this setting, the AV bundle and proximal left bundle branch will be accessible from the left or right side of the heart, and given its relatively superficial course, imaging of the central AV conduction axis by UHR-SD-OCT should be possible. During open heart surgery to repair congenital heart defects, the heart is stopped while circulation to the rest of the body is maintained by the heart-lung bypass machine. Thus, OCT has the potential to be used *in vivo* intraoperatively without blood covering the surface of the endocardium and without cardiac motion-induced artifacts. The integration of our UHR-SD-OCT system into a handheld probe would likely be most practical in such an intraoperative context. UHR-SD-OCT could then potentially be used to identify vulnerable AV conduction tissues prior to VSD patch closure and help avoid heart block during open heart surgery for repair of certain congenital heart defects.

References

1. X. Ge, S. Chen, S. Chen, and L. Liu, "High resolution optical coherence tomography," J. Lightwave Technol. **39**(12), 3824–3835 (2021).
2. L. Liu, J. A. Gardecki, S. K. Nadkarni, J. D. Toussaint, Y. Yagi, B. E. Bouma, and G. J. Tearney, "Imaging the subcellular structure of human coronary atherosclerosis using micro–optical coherence tomography," Nat. Med. **17**(8), 1010–1014 (2011).
3. P. J. Marchand, A. Bouwens, D. Szlag, D. Nguyen, A. Descloux, M. Sison, S. Coquoz, J. Extermann, and T. Lasser, "Visible spectrum extended-focus optical coherence microscopy for label-free sub-cellular tomography," Biomed. Opt. Express **8**(7), 3343–3359 (2017).
4. A. Federici and A. Dubois, "Full-field optical coherence microscopy with optimized ultrahigh spatial resolution," Opt. Lett. **40**(22), 5347–5350 (2015).
5. B. Lee, S. Chen, E. M. Moult, Y. Yu, A. Y. Alibhai, N. Mehta, C. R. Baumal, N. K. Waheed, and J. G. Fujimoto, "High-speed, ultrahigh-resolution spectral-domain OCT with extended imaging range using reference arm length matching," Trans. Vis. Sci. Tech. **9**(7), 12 (2020).
6. K.-S. Lee, K. P. Thompson, P. Meemon, and J. P. Rolland, "Cellular resolution optical coherence microscopy with high acquisition speed for in-vivo human skin volumetric imaging," Opt. Lett. **36**(12), 2221–2223 (2011).
7. X. Yao, Y. Gan, C. C. Marboe, and C. P. Hendon, "Myocardial imaging using ultrahigh-resolution spectral domain optical coherence tomography," J. Biomed. Opt. **21**(06), 1 (2016).
8. R. Yadav, K.-S. Lee, J. P. Rolland, J. M. Zavislan, J. V. Aquavella, and G. Yoon, "Micrometer axial resolution OCT for corneal imaging," Biomed. Opt. Express **2**(11), 3037–3046 (2011).
9. K. Bizheva, B. Tan, B. MacLelan, O. Kralj, M. Hajialamdari, D. Hileeto, and L. Sorbara, "Sub-micrometer axial resolution OCT for in-vivo imaging of the cellular structure of healthy and keratoconic human corneas," Biomed. Opt. Express **8**(2), 800–812 (2017).
10. B. Tan, Z. Hosseinaee, L. Han, O. Kralj, L. Sorbara, and K. Bizheva, "250 kHz, 1.5 μm resolution SD-OCT for in-vivo cellular imaging of the human cornea," Biomed. Opt. Express **9**(12), 6569–6583 (2018).
11. N. Nishizawa, H. Kawagoe, M. Yamanaka, M. Matsushima, K. Mori, and T. Kawabe, "Wavelength dependence of ultrahigh-resolution optical coherence tomography using supercontinuum for biomedical imaging," IEEE J. Sel. Top. Quantum Electron. **25**(1), 1–15 (2019).
12. S. L. Jacques, "Optical properties of biological tissues: a review," Phys. Med. Biol. **58**(11), R37–R61 (2013).
13. J. M. Schmitt, A. Knuttel, M. Yadlowsky, and M. A. Eckhaus, "Optical-coherence tomography of a dense tissue: statistics of attenuation and backscattering," Phys. Med. Biol. **39**(10), 1705–1720 (1994).
14. Laser Institute of America, American National Standard for Safe Use of Lasers, ANSI Z136.1 (2014).
15. M. Yamanaka, N. Hayakawa, and N. Nishizawa, "High-spatial-resolution deep tissue imaging with spectral-domain optical coherence microscopy in the 1700-nm spectral band," J. Biomed. Opt. **24**(07), 1 (2019).

16. M. Maria, I. B. Gonzalo, T. Feuchter, M. Denninger, P. M. Moselund, L. Leick, O. Bang, and A. Podoleanu, "Q-switch-pumped supercontinuum for ultra-high resolution optical coherence tomography," Opt. Lett. **42**(22), 4744–4747 (2017).

17. M. D. Bayleyegn, H. Makhlouf, C. Crotti, K. Plamann, and A. Dubois, "Ultrahigh resolution spectral-domain optical coherence tomography at 1.3μm using a broadband superluminescent diode light source," Opt. Commun. **285**(24), 5564–5569 (2012).

18. M. Jensen, N. M. Israelsen, M. Maria, T. Feuchter, A. Podoleanu, and O. Bang, "All-depth dispersion cancellation in spectral domain optical coherence tomography using numerical intensity correlations," Sci. Rep. **8**(1), 9170 (2018).

19. S. Kray, F. Spöler, M. Först, and H. Kurz, "High-resolution simultaneous dual-band spectral domain optical coherence tomography," Opt. Lett. **34**(13), 1970–1972 (2009).

20. K. Bizheva, B. Považay, B. Hermann, H. Sattmann, W. Drexler, M. Mei, R. Holzwarth, T. Hoelzenbein, V. Wacheck, and H. Pehamberger, "Compact, broad-bandwidth fiber laser for sub-2-μm axial resolution optical coherence tomography in the 1300-nm wavelength region," Opt. Lett. **28**(9), 707–709 (2003).

21. K. Q. Kieu, N. N. Peyghambarian, J. Klein, J. K. Barton, and A. Evans, "Ultrahigh resolution all-reflective optical coherence tomography system with a compact fiber-based supercontinuum source," J. Biomed. Opt. **16**(10), 106004 (2011).

22. I. Hartl, X. D. Li, C. Chudoba, R. K. Ghanta, T. H. Ko, J. G. Fujimoto, J. K. Ranka, and R. S. Windeler, "Ultrahigh-resolution optical coherence tomography using continuum generation in an air–silica microstructure optical fiber," Opt. Lett. **26**(9), 608–610 (2001).

23. Y.-J. You, C. Wang, Y.-L. Lin, A. Zaytsev, P. Xue, and C.-L. Pan, "Ultrahigh-resolution optical coherence tomography at 1.3 μm central wavelength by using a supercontinuum source pumped by noise-like pulses," Laser Phys. Lett. **13**(2), 025101 (2016).

24. J. F. de Boer, B. Cense, B. H. Park, M. C. Pierce, G. J. Tearney, and B. E. Bouma, "Improved signal-to-noise ratio in spectral-domain compared with time-domain optical coherence tomography," Opt. Lett. **28**(21), 2067–2069 (2003).

25. R. Leitgeb, C. K. Hitzenberger, and A. F. Fercher, "Performance of Fourier domain vs. time domain optical coherence tomography," Opt. Express **11**(8), 889–894 (2003).

26. M. A. Choma, M. V. Sarunic, C. Yang, and J. A. Izatt, "Sensitivity advantage of swept source and Fourier domain optical coherence tomography," Opt. Express **11**(18), 2183–2189 (2003).

27. M. Wojtkowski, V. J. Srinivasan, T. H. Ko, J. G. Fujimoto, A. Kowalczyk, and J. S. Duker, "Ultrahigh-resolution, high-speed, Fourier domain optical coherence tomography and methods for dispersion compensation," Opt. Express **12**(11), 2404–2422 (2004).

28. S. H. Yun, G. J. Tearney, B. E. Bouma, B. H. Park, and J. F. de Boer, "High-speed spectral-domain optical coherence tomography at 1.3 μm wavelength," Opt. Express **11**(26), 3598–3604 (2003).

29. A. F. Fercher, W. Drexler, C. K. Hitzenberger, and T. Lasser, "Optical coherence tomography—principles and applications," Rep. Prog. Phys. **66**(2), 239–303 (2003).

30. M. Jensen, I. B. Gonzalo, R. D. Engelsholm, M. Maria, N. M. Israelsen, A. Podoleanu, and O. Bang, "Noise of supercontinuum sources in spectral domain optical coherence tomography," J. Opt. Soc. Am. B **36**(2), A154 (2019).

31. L. Bernstein, A. Ramier, J. Wu, V. D. Aiello, M. J. Béland, C. P. Lin, and S.-H. Yun, "Cross-sectional UHR-SD-OCT image stack (XZ, full resolution) of porcine left bundle branch fibers," figshare (2021), https://doi.org/10.6084/m9.figshare.16639387.

32. R. H. Anderson, J. Yanni, M. R. Boyett, N. J. Chandler, and H. Dobrzynski, "The anatomy of the cardiac conduction system," Clin. Anat. **22**(1), 99–113 (2009).

33. L. Liberman, E. S. Silver, P. J. Chai, and B. R. Anderson, "Incidence and characteristics of heart block after heart surgery in pediatric patients: A multicenter study," J. Thorac. Cardiovasc. Surg. **152**(1), 197–202 (2016).

34. R. S. Mosca, "Cardiopulmonary bypass, cardioplegia, confocal inspection. . . ?" J. Thorac. Cardiovasc. Surg. **152**(1), 203–204 (2016).

35. C. M. Ambrosi, V. V. Fedorov, R. B. Schuessler, A. M. Rollins, and I. R. Efimov, "Quantification of fiber orientation in the canine atrial pacemaker complex using optical coherence tomography," J. Biomed. Opt. **17**(7), 1 (2012).

36. O. Kilinc, X. Zhao, M. Jenkins, C. Snyder, and A. Rollins, "Imaging of atrioventricular nodal conduction tissue in porcine hearts using optical coherence tomography," J. Innov. Cardiac Rhythm Manage. **10**(6), 3675–3680 (2019).

37. S. J. Crick, M. N. Sheppard, S. Y. Ho, L. Gebstein, and R. H. Anderson, "Anatomy of the pig heart: comparisons with normal human cardiac structure," J. Anat. **193**(1), 105–119 (1998).

38. R. D. S. Shreesha, M. Jensen, L. Grüner-Nielsen, J. T. Olsen, P. Heiduschka, B. Kemper, J. Schnekenburger, M. Glud, M. Mogensen, N. M. Israelsen, and O. Bang, "Shot-noise limited, supercontinuum-based optical coherence tomography," Light: Sci. Appl. **10**(1), 133 (2021).

39. X. Ji, D. Mojahed, Y. Okawachi, A. L. Gaeta, C. P. Hendon, and M. Lipson, "Millimeter-scale chip–based supercontinuum generation for optical coherence tomography," Sci. Adv. **7**(38), abg8869 (2021).

40. J. Ai and L. V. Wang, "Spectral-domain optical coherence tomography: removal of autocorrelation using an optical switch," Appl. Phys. Lett. **88**(11), 111115 (2006).

41. E. Bo, Y. Luo, S. Chen, X. Liu, N. Wang, X. Ge, X. Wang, S. Chen, S. Chen, J. Li, and L. Liu, "Depth-of-focus extension in optical coherence tomography via multiple aperture synthesis," Optica **4**(7), 701–706 (2017).

42. M. Lev, "Conduction system in congenital heart disease," Am. J. Cardiol. **21**(5), 619–627 (1968).

43. J. P. Moore and J. A. Aboulhosn, "Introduction to the congenital heart defects: anatomy of the conduction system," Card. Electrophysiol. Clin. **9**(2), 167–175 (2017).